# High speed single- and dual-stage vertical positioners

Yuen K. Yong, Sachin P. Wadikhaye, and Andrew J. Fleming

Citation: Review of Scientific Instruments **87**, 085104 (2016); doi: 10.1063/1.4960080
View online: http://dx.doi.org/10.1063/1.4960080
View Table of Contents: http://scitation.aip.org/content/aip/journal/rsi/87/8?ver=pdfcov
Published by the AIP Publishing

**Articles you may be interested in**

A novel flexure-based vertical nanopositioning stage with large travel range
Rev. Sci. Instrum. **86**, 105112 (2015); 10.1063/1.4932963

Design and experimental tests of a dual-servo piezoelectric nanopositioning stage for rotary motion
Rev. Sci. Instrum. **86**, 045002 (2015); 10.1063/1.4918295

Development of compact high precision two degree of freedom X Y piezoelectric stepping positioner
Rev. Sci. Instrum. **79**, 026110 (2008); 10.1063/1.2841807

High bandwidth nano-positioner: A robust control approach
Rev. Sci. Instrum. **73**, 3232 (2002); 10.1063/1.1499533

A fast high-voltage amplifier for driving piezoelectric positioners
Rev. Sci. Instrum. **71**, 4323 (2000); 10.1063/1.1319984

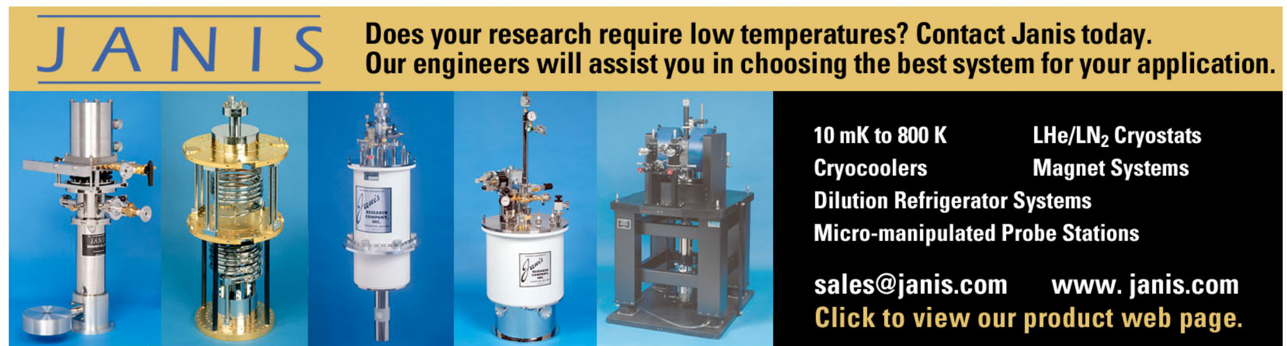


Reuse of AIP Publishing content is subject to the terms at: https://publishing.aip.org/authors/rights-and-permissions. Download to IP: 134.148.193.166 On: Mon, 08 Aug 2016 05:17:24

# High speed single- and dual-stage vertical positioners

Yuen K. Yong,[a] Sachin P. Wadikhaye,[b] and Andrew J. Fleming[c]
*School of Electrical Engineering and Computer Science at The University of Newcastle, Callaghan, NSW, Australia*

(Received 17 November 2015; accepted 18 July 2016; published online 5 August 2016)

This article presents a high-speed single- and dual-stage vertical positioners for applications in optical systems. Each positioner employs a unique end-constraint method with orthogonal flexures to preload a piezoelectric stack actuator. This end-constraint method also significantly increases the first mechanical resonance frequency. The single-stage positioner has a displacement range of 7.6 $\mu$m and a first resonance frequency of 46.8 kHz. The dual-stage design consists of a long-range slow-stage and a short-range fast-stage. An inertial counterbalance technique was implemented on the fast-stage to cancel inertial forces resulting from high-speed motion. The dual-stage positioner has a combined travel range of approximately 10 $\mu$m and a first evident resonance frequency of 130 kHz. *Published by AIP Publishing.* [http://dx.doi.org/10.1063/1.4960080]

## I. INTRODUCTION

High-speed piezoelectric nanopositioning systems have been the positioner of choice in many applications including scanning probe microscopy,[1–4] beam steering systems,[5,6] nanofabrication,[7] and optical fiber alignment.[8] Most of these high-speed nanopositioners are flexure-guided systems where fine motions were produced through elastic deformation of flexures. There are no joints and gears in these systems thus eliminating issues such as friction, wear, and backlash.[9,10] These characteristics allow flexure-guided mechanisms to generate smooth and repeatable motions, which are prerequisite for nanometer precision applications.[11]

There is demand for high-speed single-axis nanopositioners in optical applications such as cavity tuning in continuous-wave lasers and cavity ring-down spectroscopy.[12–16] High-speed vertical positioners are also utilized to lock the phase of closed-loop Michelson interferometers.[17]

The bandwidth of the aforementioned optical systems is often governed by the bandwidth of the piezo-stage. One of the simplest ways of moving a mirror vertically is to attach it to a piezo-stack actuator [see Fig. 1]. However, this arrangement may not be suitable for high-speed positioning applications. Piezo-stack actuators are highly sensitive to tensile forces. The excessive inertial (tensile) forces experienced during high-speed motion can damage the actuator.[18,19] To protect the actuator, preload is applied to the actuator to compensate for these excessive forces at high speeds. Some preloading techniques also help to increase the first resonance frequency of positioners.[2,11]

There are several end-constraint methods for piezo-stack actuators to improve their performance at high speeds. One common way is to use a flexural mechanism to preload the actuator.[11] Circular plate and diaphragm flexures have also been used to preload and guide the motion of stack actuators.[2,3,20] These systems also incorporate inertial cancellation techniques to passively suppress the first actuation mode which increases the mechanical bandwidth. Details for inertial cancellation techniques can be found in Ando *et al.*,[21] Kenton *et al.*,[2] and Yong and Moheimani.[22]

Table I summarizes the performance of various vertical stage designs in terms of travel range and speed. Three-axis stages, which translate along the x, y, and z axes, are also included. However, only the travel range and speed of the z-axis are compared. For single-axis stage, the micro-positioning tower[23] has the largest travel range of 200 $\mu$m but a bandwidth of only 256 Hz which may not be suitable for optical applications. This is expected due to the direct trade-off between travel range and resonance frequency. The three-axis stage design from Ando *et al.*[21] has the fastest z-axis, however, with a travel range of only 2 $\mu$m.

To simultaneously obtain a large travel range and wide bandwidth, the dual-actuation configuration combines a short-range, fast-stage and a long-range, slow-stage.[2,4,20,27] These referenced dual-stage designs are for atomic force microscopy (AFM). However, the term "dual-stage" in these literatures refers to the driving and control method of the slow- and fast-stage rather than the physical design of the stage. All the reported designs are actually short-range stages operated in conjunction with an external long-range nanopositioner. Schitter *et al.*[27] and Fleming[4] utilize a piezo-stack actuator in conjunction with a piezoelectric tube scanner to provide fast actuation during AFM imaging. However, the actuator may experience a high tensile load at high speed which reduces the life of the actuator. Kenton *et al.*[2] and Fleming *et al.*[20] utilize a circular flexure to constrain and preload the actuator. These flexure-guided designs increase the dominant resonance frequency of the fast-stage to above 100 kHz, albeit with a range in the single microns. Again, this fast-stage operates in collaboration with an external long-range stage.

This article proposes two single-axis high-speed vertical positioners driven for optical applications. These positioners have unique end-constraint designs to increase the mechan-

[a]Electronic mail: yuenkuan.yong@newcastle.edu.au
[b]Electronic mail: swadikhaye@gmail.com
[c]Electronic mail: andrew.fleming@newcastle.edu.au



Reuse of AIP Publishing content is subject to the terms at: https://publishing.aip.org/authors/rights-and-permissions. Download to IP: 134.148.193.166 On: Mon, 08 Aug 2016 05:17:24

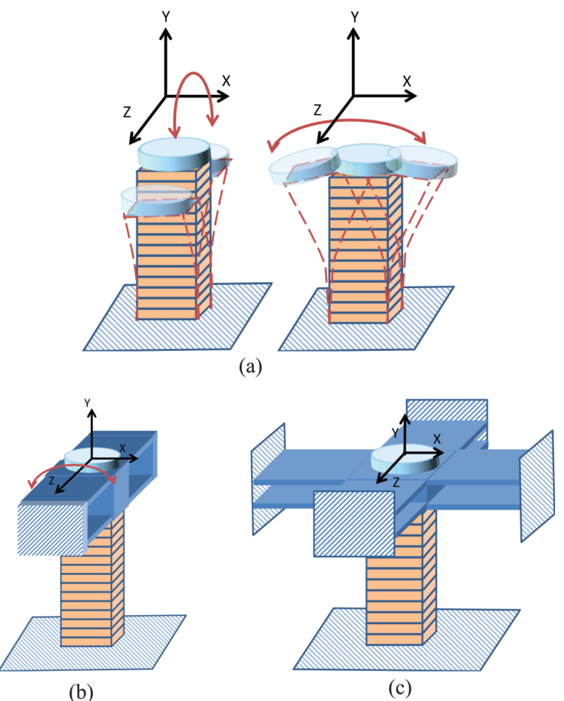


FIG. 1. Different configurations for the design of nanopositioning systems: (a) a mirror is attached to the piezo-stack actuator directly without end-constraints. (b) A set of flexures is used to constrain the piezo-stack actuator. (c) Two sets of orthogonal flexures are used to constrain the piezo-stack actuator.

ical bandwidth and preload the actuator. The first design is a single-stage positioner which has a first mechanical resonance frequency of 47 kHz and a large travel range of 7.6 $\mu$m. The second design has a dual-stage configuration where a fast-stage with short travel range is mounted to a slow-stage with a long travel range. The dual-stage positioner has a first evident resonance frequency of 130 kHz and a combined travel range of approximately 10 $\mu$m.

The proposed single-stage design achieves a relatively large travel range and bandwidth simultaneously, which is suitable for optical applications. The dual-stage design integrates both slow- and fast-stages into one structure without the need of an external long-range stage. Furthermore, an inertial counterbalance technique is incorporated in the fast-stage design to cancel vibrations. To the authors' knowledge, the proposed dual-stage design principle has not yet been reported.

The remainder of this article proceeds as follows. Sec. II describes the mechanical design of the two positioners together with analytical and finite-element models of the dynamics. Sec. III presents the control design for the dual-stage positioner. Experimental results of the two positioners are presented in Sec. IV followed by conclusions in Sec. V.

TABLE I. Summary of vertical stage designs.

| Nanopositioner | Range ($\mu$m) | Dominant res. (kHz) |
|---|---|---|
| Single-axis stage | | |
| Jouaneh and Ge[23] | 200 | 0.256 |
| Single-stage (this article) | 7.6 | 47 |
| Three-axis stage[a] | | |
| Ando *et al.*[21] | 2 | 171 |
| Watanabe *et al.*[24] | 2.5 | 100 |
| Kenton and Leang[25] | 1 | 70 |
| Schitter *et al.*[26] | 4.3 | 22 |
| Single-axis stage used in dual-actuation[b] | | |
| Kenton *et al.*[2] | 1.56 | 150 |
| Fleming *et al.*[20] | 2.3 | 103 |
| Schitter *et al.*[27] | n/a | 80 |
| Fleming[4] | 1 | 23 |
| Single-axis, dual-stage | | |
| Dual-stage (this article) | 0.922 (fast) | 130 |
| | 9.4 (slow) | 17 |

[a]These are three-axis stages. Only the performance of the z-axis is listed here.
[b]These are short-range stages. They are operated in collaboration with an external AFM long-range nanopositioner.

## II. MECHANICAL DESIGN AND ANALYSIS

A slender piezo-stack actuator is subject to two bending modes in the x and z axes, respectively, as shown in the left column of Fig. 1. To increase the mechanical bandwidth, it is desirable to increase the resonance frequency of these bending modes. A set of flexures as illustrated in the middle column of Fig. 1 constrains only one of these bending modes. In order to constrain both bending modes, two sets of orthogonal flexures as shown in the right column of Fig. 1 are used in the proposed single- and dual-stage positioners. Double-hinged flexures (see Fig. 2) which have high out-of-plane stiffness[25,28] are desirable candidates for the vertical positioner designs. When they are arranged in the configuration shown in the right column of Fig. 1, the stiffness in the x and z axes can be increased significantly, which increases the resonance frequencies.

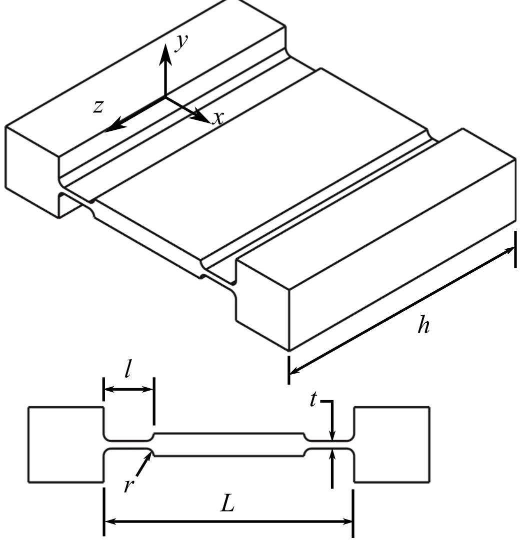


FIG. 2. Double-hinged flexure and its dimensions.

Reuse of AIP Publishing content is subject to the terms at: https://publishing.aip.org/authors/rights-and-permissions. Download to IP: 134.148.193.166 On: Mon, 08 Aug 2016 05:17:24

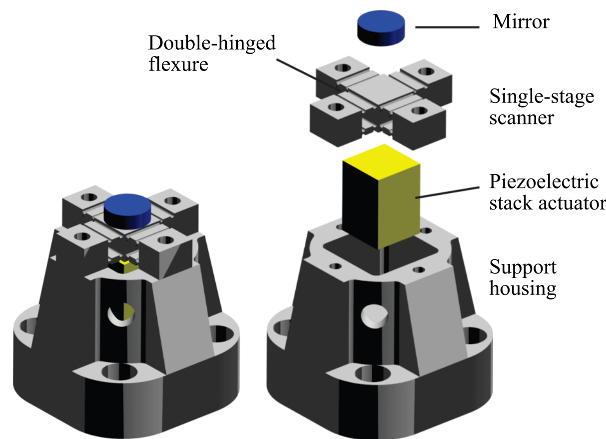


FIG. 3. Single-stage positioner and its exploded view.

## A. Single-stage positioner design

The single-stage vertical positioner is illustrated in Fig. 3. The mirror stage is supported by eight parallel double-hinged flexures arranged using the orthogonal configuration in Fig. 1(c). A piezo-stack actuator (7 mm × 7 mm × 10 mm) is used to elastically deform the flexures, which drives the mirror vertically. Both the flexure-based positioner and the piezo-stack are mounted to a support housing. The flexures and the support housing are constructed from aluminum alloy 7075 and stainless steel 304, respectively. Their material properties can be found in Table II.

### *1. Stiffness and range estimation*

To estimate the compliance of the double-hinged flexures, the in-plane deformations of the hinge can be expressed in a matrix form,[9] that is,

$$\begin{Bmatrix} u_x \\ u_y \\ \theta_z \end{Bmatrix} = \begin{bmatrix} C_{x-F_x} & 0 & 0 \\ 0 & C_{y-F_y} & C_{y-M_z} \\ 0 & C_{\theta_z-F_y} & C_{\theta_z-M_z} \end{bmatrix} \begin{Bmatrix} F_x \\ F_y \\ M_z \end{Bmatrix}, \tag{1}$$

where $C_{\theta_z-F_y} = C_{y-M_z}$. The in-plane compliances are

$$C_{x-F_x} = \frac{1}{Eh}\int_0^L \frac{1}{t(x)}dx, \tag{2}$$

$$C_{y-F_y} = \frac{12}{Eh}\int_0^L \frac{x^2}{t(x)^3}dx + \frac{\alpha E}{G}C_{x-Fx}, \tag{3}$$

$$C_{y-M_z} = \frac{12}{Eh}\int_0^L \frac{x}{t(x)^3}dx, \tag{4}$$

$$C_{\theta_z-M_z} = \frac{12}{Eh}\int_0^L \frac{1}{t(x)^3}dx, \tag{5}$$

where $h$ is the depth of the flexure, $L$ is the entire length of the flexure, $E$ is the Young modulus, $G = \frac{E}{2(1+\nu)}$ is the shear modulus, and $\alpha$ is the shear coefficient. The dimensions of the flexure are reported in Fig. 2. $t(x)$ is the thickness of the flexure

TABLE II. Design parameters, dimensions and material properties of the single- and dual-stage vertical positioners.

| Material properties | Aluminum alloy 7075 | Stainless steel 304 | |
|---|---|---|---|
| Young's modulus, $E$ (GPa) | 72 | 200 | |
| Poisson's ratio, $\upsilon$ | 0.33 | 0.3 | |
| Density, $\rho$ (kg/m$^3$) | 2770 | 7850 | |
| **Single-stage vertical positioner** | | | |
| Double-hinge flexure | | Piezo-stack actuator | |
| Thickness, $t$ (mm) | 0.3 | Cross-sectional area, $A_a$ (mm) | 7×7 |
| Depth, $h$ (mm) | 5.5 | Length, $l_a$ (mm) | 10 |
| Flexure length, $l$ (mm) | 0.6 | Young's modulus, $E_a$ (GPa) | 33 |
| Entire flexure length, $L$ (mm) | 2.5 | Nominal stroke, $\Delta l_o$ ($\mu$m) | 10 |
| Corner-fillet radius, $r$ (mm) | 0.25 | | |
| **Dual-stage vertical positioner** | | | |
| Slow-stage - double-hinged flexure | | Fast-stage - square plate flexure | |
| Thickness, $t$ (mm) | 0.2 | Plate thickness, $t_p$ (mm) | 0.35 |
| Depth, $h$ (mm) | 10 | Side length (mm) | 12 |
| Flexure length, $l$ (mm) | 0.7 | Effective side length, $a$ (mm) | 8.5 |
| Entire flexure length, $L$ (mm) | 3 | | |
| Corner-fillet radius, $r$ (mm) | 0.1 | | |
| Long-range piezo-stack | | Short-range piezo-stack | |
| Cross-sectional area, $A_a$ (mm) | 7×7 | Cross-sectional area, $A_a$ (mm) | 5×5 |
| Length, $l_a$ (mm) | 10 | Length, $l_a$ (mm) | 2 |
| Young's modulus, $E_a$ (GPa) | 33 | Young's modulus, $E_a$ (GPa) | 33 |
| Nominal stroke, $\Delta l_o$ ($\mu$m) | 10 | Nominal stroke, $\Delta l_o$ ($\mu$m) | 1.9 |

Reuse of AIP Publishing content is subject to the terms at: https://publishing.aip.org/authors/rights-and-permissions. Download to IP: 134.148.193.166 On: Mon, 08 Aug 2016 05:17:24

which varies along $x$ and is expressed as[29,30]

$$t(x) = \begin{cases} t + 2\left[r - \sqrt{x(2r-x)}\right] & ,x \in [0,a] \\ t & ,x \in [a,b] \\ t + 2\left[r - \sqrt{(l-x)(2r-l+x)}\right] & ,x \in [b,c] \\ t + 2r & ,x \in [c,d], \\ t + 2\left[r - \sqrt{(l-g)(2r-l+g)}\right] & ,x \in [d,e] \\ t & ,x \in [e,f] \\ t + 2\left[r - \sqrt{g(2r-g)}\right] & ,x \in [f,L] \end{cases} \quad (6)$$

where $a = r, b = l - r, c = l, d = L - l, e = d + r, f = L - r, g = L - x$, $t$ and $l$ are the thickness and the length of the thin section of the flexure, $r$ is the fillet radius, and $L$ is the length of the entire flexure. For a fixed-guided hinge with a concentrated load, the resultant moment is $-F_y L/2$. According to Eq. (1), the deformation $u_y$ due to $F_y$ and $M_z$ is

$$\begin{aligned} u_y &= C_{y-Fy}F_y + C_{y-Mz}M_z \\ &= C_{y-Fy}F_y + C_{y-Mz}\left[\frac{-F_y L}{2}\right]. \end{aligned} \quad (7)$$

By substituting Eqs. (3), (4), and (6) into (7), and solving it numerically by taking the ratio of force to deflection (see Table II for design parameters and values), the bending stiffness $k_y$ is calculated to be 0.94 N/$\mu$m. Since there are eight hinges arranged in parallel, the total stiffness of the positioner along the y-direction (vertical) is $K_s = 8 \times k_y = 9.5$ N/$\mu$m. This is approximately 4.6% of the stiffness of the actuator ($k_a = E_a A_a / L_a$). For a 10-$\mu$m range piezo-stack, the resultant stroke $\Delta l_a$ of the actuator pushing against the flexures is

$$\begin{aligned} \Delta l_a &= \Delta l_o \frac{k_a}{k_a + K_s} \\ &= 9.6\ \mu m, \end{aligned} \quad (8)$$

where $\Delta l_o$ is the nominal stroke of the piezo-actuator.

### 2. Finite-element-analysis (FEA)

Finite-element-analysis (FEA) of the single-stage positioner was carried out using ANSYS workbench. To estimate the stiffness, the static analysis module in ANSYS was used. The four mounting holes of the positioner as shown in Fig. 4 were fixed. Force was then applied to the central platform and the corresponding deformation was obtained. Stiffness of the single-stage positioner was calculated from the ratio of the applied force to the deformation, which is 8.3 N/$\mu$m. This result is in close agreement with that of the analytical result.

Modal analysis was carried out in ANSYS to estimate the resonance frequencies of the single-stage positioner. When conducting modal analysis, the bottom surface of the support housing is fixed. A mirror with a diameter of 6 mm, a thickness of 2 mm, and a mass of 0.5 g were attached to the single-stage. This mirror is expected to be the worst case payload. Fig. 5 compares the resonance frequencies of a piezo-stack actuator and mirror with different flexure configurations. It can be observed that orthogonal flexures provide the greatest

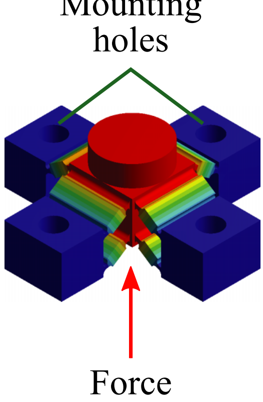


FIG. 4. Finite-element simulated stiffness of the single-stage positioner.

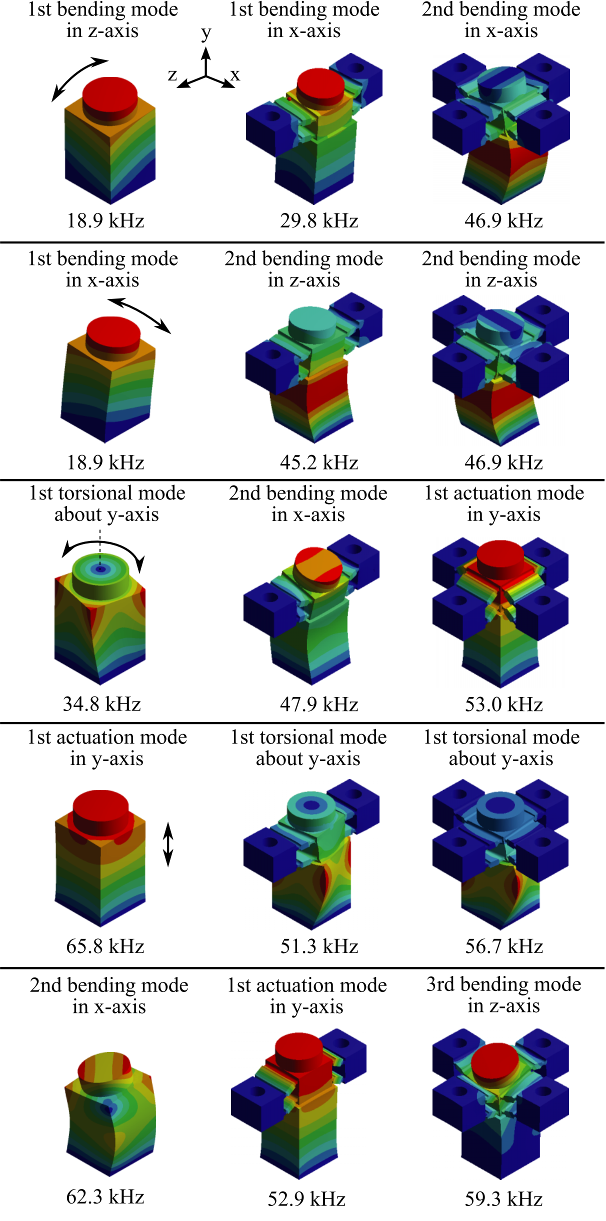


FIG. 5. Resonance frequencies of the single-stage vertical positioner. In the left column, a mirror is mounted on a piezo-stack actuator without flexures. In the middle column, a piezo-stack actuator is constrained by four double-hinged flexures connected in parallel. In the right column, a piezo-stack actuator is constrained by eight double-hinged flexures. The resonance frequencies can be observed to be significantly higher with eight flexures.

Reuse of AIP Publishing content is subject to the terms at: https://publishing.aip.org/authors/rights-and-permissions. Download to IP: 134.148.193.166 On: Mon, 08 Aug 2016 05:17:24

increase in resonance frequencies. Note that the support housing is hidden in the simulated results in order to show the mode shapes of the piezo-stack actuator.

The first bending mode in the x and z axes of the piezo-stack appears at 18.9 kHz, respectively. By constraining the piezo-stack using one set of the double-hinged flexures, its first bending mode in the z-axis is eliminated. The first bending mode in the x-axis is increased from 18.9 kHz to 29.8 kHz. Its subsequent modes are shifted to above 45 kHz. The first bending modes in both x and z axes of the piezo-stack vanish when the actuator is constrained using the proposed orthogonal flexures. The first appearance of a resonance mode is the second bending mode at 46.9 kHz (in both x and z axes). The actuation mode appears at 53 kHz, which is slightly lower compared to that of the piezo-stack without end-constraint (at 65.8 kHz). This is associated with the increase of effective mass due to the flexures and moving platform. However, its preceding modes have been significantly increased to above 46 kHz.

## B. Dual-stage positioner design

To achieve even higher mechanical bandwidth than 47 kHz, the dual-stage positioner shown in Fig. 6 was developed. This consists of fast and slow stages made from aluminum alloy 7075. The slow-stage is supported by 12 double-hinged flexures arranged in an orthogonal configuration as previously discussed in Sec. II A. This configuration is used to increase the resonance frequency of the bending modes. A 7 mm × 7 mm × 10 mm piezo-stack is used to drive the slow-stage.

The fast-stage is driven by a 5 mm × 5 mm × 2 mm piezo-stack actuator. The piezo-stack is sandwiched by two 0.5-$\mu$m alumina plates. A thin plate flexure is used to guide the motion of the piezo-stack along the direction of actuation. During high-speed operation, the fast movement of the piezo-stack generates inertial forces which tend to excite the resonance frequency of the slow-stage. To compensate for these forces, an inertial counterbalance technique is employed where two piezo-stack actuators displace with the same magnitude but opposite directions.[1–3] The dummy mass is chosen to be approximately the same as the mass of the mirror.

The slow- and fast-stages are connected together by the spacer shown in Fig. 6. This aluminum structure transmits force from the slow-stage to the body of the fast-stage without contacting the counterbalance mechanism. The slow-stage and the long-range piezo-stack are both mounted to a base which is made from stainless steel 304.

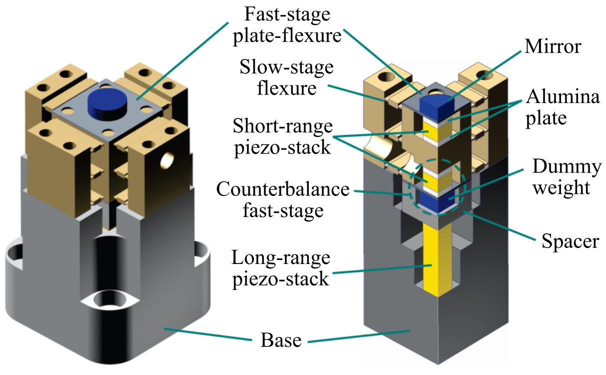


FIG. 6. Dual-stage vertical positioner.

### 1. Stiffness and range estimation

Using a similar method to that discussed in Sec. II A, the stiffness and range of the slow-stage were calculated to be 3 N/$\mu$m and 9.8 $\mu$m, respectively. For the fast-stage, the vertical stiffness of the square plate flexure can be calculated using plate theory. Assuming a uniform load applied to the plate, the maximum deformation is[31]

$$\delta_y = \frac{\alpha_p q a^4}{E t_p^3} = \frac{\alpha_p F a^2}{E t_p^3}, \tag{9}$$

where $\alpha_p = 0.0138$ (for a square plate), $q = F/a^2$ is load per unit area, $a$ is the effective width of the plate, and $t_p$ is the thickness of the plate. Note that the total side length of the plate is 12 mm and approximately 1.75-mm of material from each side of the plate is glued to the slow-stage. As a result, the effective length $a = 8.5$ mm is used in Eq. (9) and the estimated stiffness of the plate flexure is 3.1 N/$\mu$m.

### 2. Finite-element-analysis

Finite-element simulated stiffness of each stage was found using similar technique showed in Fig. 4. A unit force was applied to the central platforms of each stage. The mounting holes of each stage were fixed. Deformation of the central platform was recorded to calculate the stiffness. The simulated stiffness of the slow and fast-stage is 3.3 N/$\mu$m and 2.5 N/$\mu$m, respectively, which are in close agreement to that of the analytical calculations.

Modal analysis was carried out to search for the resonance frequencies of the actuation modes. The bottom surface of the base was fixed when conducting the modal analysis. A mirror, which has a mass of 0.5 g, was attached to the moving platform of the dual-stage to account for the worst payload of the system in practice. Fig. 7 reveals the two actuation modes of the positioner. The sectional views of the FEA results show the mode shapes of the dual-stage positioner. The first actuation mode appears at 20 kHz which is caused by the slow-stage positioner. The second actuation mode is caused by the fast-stage positioner which appears at 104 kHz.

## III. DUAL-STAGE CONTROL

The goal of a dual-stage controller is to operate the slow- and fast-stage mechanisms collaboratively.[19] A number of model based methods have been proposed;[32,33] however, due to the required bandwidth in this application, the complementary filter method[34] illustrated in Fig. 8 is desirable. This method does not provide optimal range utilization but can be imple-

Reuse of AIP Publishing content is subject to the terms at: https://publishing.aip.org/authors/rights-and-permissions. Download to IP: 134.148.193.166 On: Mon, 08 Aug 2016 05:17:24

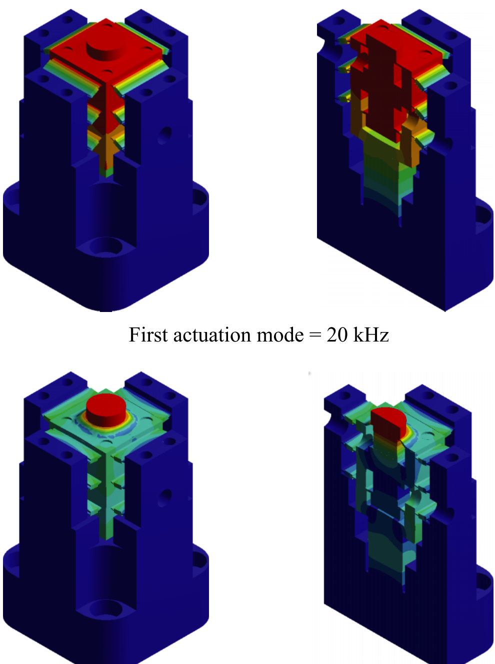


FIG. 7. Actuation modes of the dual-stage vertical positioner.

mented with a first-order analog circuit, which is advantageous in high bandwidth applications.

In Fig. 8, the displacement transfer function is

$$\frac{d(s)}{r(s)} = \alpha F_{HP}(s) K_{fast} + F_{LP}(s) K_{slow}, \tag{10}$$

where $r(s)$ is the input signal, and $K_{fast}$ and $K_{slow}$ are the fast- and slow-stage sensitivities from the power amplifier input to the displacement in nm. If the gain $\alpha$ is chosen equal to $K_{slow}/K_{fast}$, both signal paths will have a sensitivity equal to $K_{slow}$. Therefore, the displacement transfer function becomes

$$\frac{d(s)}{r(s)} = K_{slow}\left(F_{HP}(s) + F_{LP}(s)\right). \tag{11}$$

If the filters $F_{HP}(s)$ and $F_{HP}(s)$ are chosen to be complementary, that is, they sum to unity, then the dual stage-response is constant with respect to frequency. In this work, the filters are chosen to be first-order,

$$F_{HP}(s) = \frac{s}{s + 2\pi f_t}, \quad F_{LP}(s) = \frac{2\pi f_t}{s + 2\pi f_t}, \tag{12}$$

where $f_t$ is the transition frequency which must be significantly lower than the slow-stage resonance frequency. With

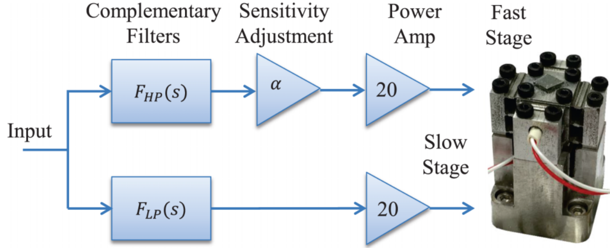


FIG. 8. The dual-stage control method based on complementary filters.

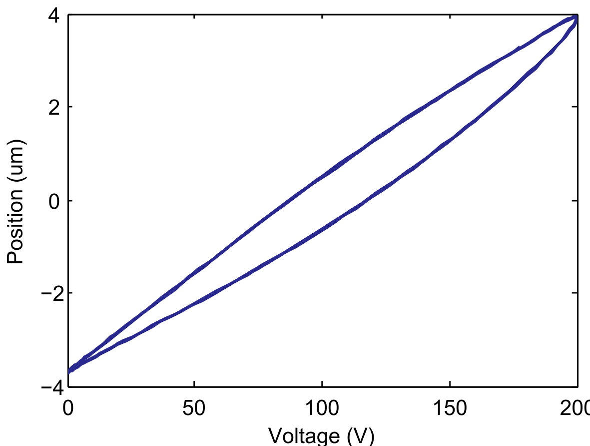


FIG. 9. Input-output response of the single-stage positioner at full range.

this configuration, the dual-stage response is dominated by the slow-stage at frequencies below $f_t$ and the fast-stage at frequencies above $f_t$.

## IV. EXPERIMENTAL RESULTS

### A. Single-stage positioner

The displacement of the single-stage positioner was measured using an Attocube FPS3010 fiber interferometer. The positioner developed a maximum travel range of 7.63 $\mu$m when driven with a 100-Hz 200-Vp-p sinusoid using a PD200 voltage amplifier. The input-output response is plotted in Fig. 9. The travel range has been reduced by approximately 20% from 10 $\mu$m to 7.63 $\mu$m due to the preload. However, the proposed preload technique has significantly increased the first resonance frequency which justifies the reduction in range.

The frequency response was measured with an in-house high-bandwidth interferometer[17] and is plotted in Fig. 10. The

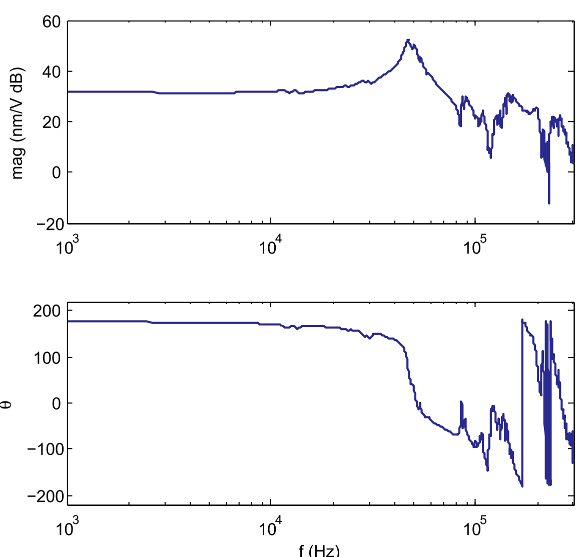


FIG. 10. Frequency response of the single-stage vertical positioner (in nm/V).

Reuse of AIP Publishing content is subject to the terms at: https://publishing.aip.org/authors/rights-and-permissions. Download to IP: 134.148.193.166 On: Mon, 08 Aug 2016 05:17:24

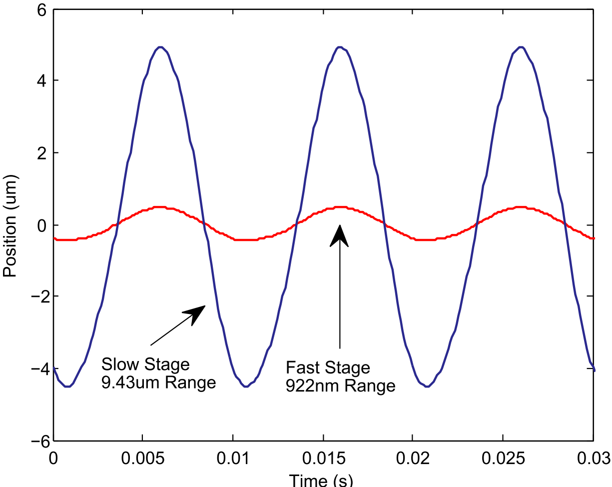


FIG. 11. Maximum range of the slow and fast stages of the dual-stage vertical positioner.

first resonance frequency of the vertical positioner is observed at 47 kHz, which is slightly higher than the predicted value of 41 kHz.

## B. Dual-stage positioner

The full-range displacement of the slow and fast stages is plotted in Fig. 11. The frequency responses of the individual stages and the dual-stage response are plotted in Fig. 12. The slow-stage has a first resonance frequency of 17 kHz, while the fast-stage has a first resonance frequency of 130 kHz. Since the slow-stage resonance frequency is avoided by the complimentary filters, the first evident resonance frequency is that of the fast-stage. In addition to the primary resonance modes, some extremely low profile modes can be observed in the response of both positioners. These modes are not predicted by the model and are thought to be modes of the support structures.

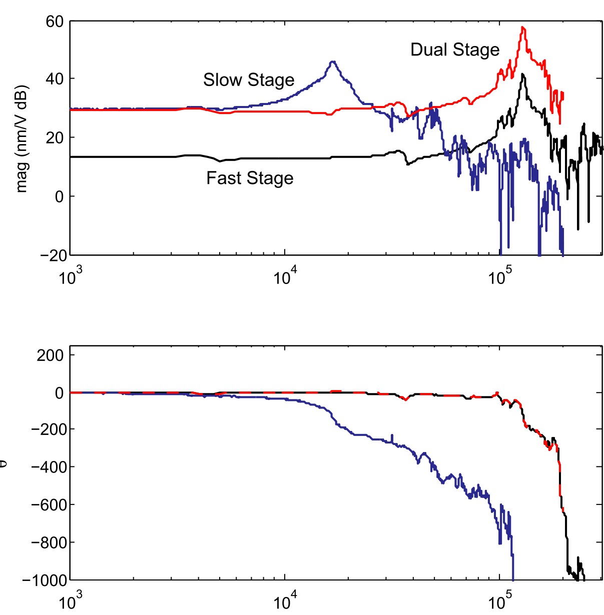


FIG. 12. Frequency responses of the dual-stage vertical positioner.

The transition frequency $f_t$ of the dual-stage controller is chosen to be 500 Hz which avoids significant excitation of the slow-stage resonance frequency. The maximum travel range is approximately 9.4 $\mu$m at frequencies below 500 Hz and 922 nm at frequencies higher than 500 Hz.

## V. CONCLUSIONS

This article describes high-speed single- and dual-stage flexure-guided vertical positioners. A unique end-constraint method with orthogonal flexures was designed to preload the piezo-stack actuator as well as to suppress its first bending mode in the x and z axes, respectively. By using the orthogonal sets of flexures, the first resonance mode of the single-stage positioner was increased from 18.9 kHz to 46.8 kHz, an improvement of 2.5 times. To achieve even higher bandwidth than 47 kHz, a dual-stage positioner was developed which incorporates a short-range fast positioner and long-range slow positioner. The fast-stage employs an inertial counterbalance technique to reduce the excitation of slow-stage dynamics. The dual-stage positioner has a first evident resonance frequency of 130 kHz and a combined travel range of approximately 10 $\mu$m. The two proposed vertical positioners are suitable for many high-speed applications in optical systems, including phase-shifting in tunable lasers, and phase-locking in laser interferometry.

## ACKNOWLEDGMENTS

This work was supported by the Australian Research Council DECRA Project No. DE130100879 and the Discovery Project No. DP150103521.

[1]T. Ando, "High-speed atomic force microscopy coming of age," Nanotechnology **23**(6), 062001 (2012).
[2]B. J. Kenton, A. J. Fleming, and K. K. Leang, "Compact ultra-fast vertical nanopositioner for improving scanning probe microscope scan speed," Rev. Sci. Instrum. **82**(12), 123703 (2011).
[3]Y. K. Yong and S. O. R. Moheimani, "Design of an inertially counterbalanced Z-nanopositioner for high-speed atomic force microscopy," IEEE/ASME Trans. Nanotechnol. **12**(2), 137–145 (2013).
[4]A. Fleming, "Dual-stage vertical feedback for high-speed scanning probe microscopy," IEEE Trans. Control Syst. Technol. **19**(1), 156–165 (2011).
[5]G. Genoud, F. Wojda, M. Burza, A. Persson, and C.-G. Wahlström, "Active control of the pointing of a multi-terawatt laser," Rev. Sci. Instrum. **82**(3), 033102 (2011).
[6]J. J. Gorman, N. G. Dagalakis, and B. G. Boone, "Multi-loop control of nanopositioning mechanism for ultra-precision beam steering," Proc. SPIE **5160**, 170–181 (2004).
[7]A. A. Tseng, S. Jou, A. Notargiacomo, and T. Chen, "Recent developments in tip-based nanofabrication and its roadmap," J. Nanosci. Nanotechnol. **8**, 2167–2186 (2008).
[8]Z. Wang, L. Chen, and L. Sun, "An integrated parallel micromanipulator with flexure hinges for optical fiber alignment," in *ICMA 2007 International Conference on Mechatronics and Automation, August 2007* (IEEE, 2007), pp. 2530–2534.
[9]N. Lobontiu, *Compliant Mechanisms: Design of Flexure Hinges* (CRC Press, 2003).
[10]L. Howell, *Compliant Mechanisms* (John Wiley & Sons, Inc, 2001).

Reuse of AIP Publishing content is subject to the terms at: https://publishing.aip.org/authors/rights-and-permissions. Download to IP: 134.148.193.166 On: Mon, 08 Aug 2016 05:17:24

[11]Y. K. Yong, S. O. R. Moheimani, B. J. Kenton, and K. K. Leang, "Invited review article: High-speed flexure-guided nanopositioning: Mechanical design and control issues," Rev. Sci. Instrum. **83**(12), 121101 (2012).
[12]G. Berden, R. Peeters, and G. Meijer, "Cavity ring-down spectroscopy: Experimental schemes and applications," Int. Rev. Phys. Chem. **19**(4), 565–607 (2000).
[13]I. Debecker, A. Mohamed, and D. Romanini, "High-speed cavity ringdown spectroscopy with increased spectral resolution by simultaneous laser and cavity tuning," Opt. Express **13**(8), 2906–2915 (2005).
[14]A. Cygan, D. Lisak, P. Masłowski, K. Bielska, S. Wójtewicz, J. Domysławska, R. S. Trawiński, R. Ciuryło, H. Abe, and J. T. Hodges, "Pound-drever-hall-locked, frequency-stabilized cavity ring-down spectrometer," Rev. Sci. Instrum. **82**(6), 063107 (2011).
[15]S. Z. S. Hassen, M. Heurs, E. H. Huntington, I. R. Petersen, and M. R. James, "Frequency locking of an optical cavity using linear-quadratic Gaussian integral control," J. Phys. B: At., Mol. Opt. Phys. **42**(17), 175501 (2009).
[16]N. Seymour-Smith, P. Blythe, M. Keller, and W. Lange, "Fast scanning cavity offset lock for laser frequency drift stabilization," Rev. Sci. Instrum. **81**(7), 075109 (2010).
[17]A. J. Fleming, B. Routley, and J. L. Holdsworth, "A closed-loop phase-locked interferometer for wide bandwidth position sensing," in *Proceedings of IEEE Multi-Conference on Systems and Control*, *Sydney* (IEEE, 2015).
[18]Y. K. Yong, "A new preload mechanism for a high-speed piezoelectric stack nanopositioner," Mechatronics **36**, 159–166 (2016).
[19]A. J. Fleming and K. K. Leang, *Design, Modeling and Control of Nanopositioning Systems* (Springer, London, UK, 2014).
[20]A. J. Fleming, B. J. Kenton, and K. K. Leang, "Bridging the gap between conventional and video-speed scanning probe microscopes," Ultramicroscopy **110**(9), 1205–1214 (2010).
[21]T. Ando, T. Uchihashi, N. Kodera, D. Yamamoto, A. Miyagi, M. Taniguchi, and H. Yamashita, "High-speed AFM and nano-visualization of biomolecular processes," Pflugers Arch. Eur. J. Physiol. **456**(1), 211–225 (2008).
[22]Y. K. Yong and S. O. R. Moheimani, "Collocated z-axis control of a high-speed nanopositioner for video-rate atomic force microscopy," IEEE Trans. Nanotechnol. **14**(2), 338–345 (2015).
[23]M. Jouaneh and P. Ge, "Modeling and control of a micro-positioning tower," Mechatronics **7**(5), 465–478 (1997).
[24]H. Watanabe, T. Uchihashi, T. Kobashi, M. Shibata, J. Nishiyama, R. Yasuda, and T. Ando, "Wide-area scanner for high-speed atomic force microscopy," Rev. Sci. Instrum. **84**(5), 053702 (2013).
[25]B. J. Kenton and K. K. Leang, "Design and control of a three-axis serial-kinematic high-bandwidth nanopositioner," IEEE/ASME Trans. Mechatronics **17**(2), 356–368 (2012).
[26]G. Schitter, K. J. Åstrom, B. DeMartini, P. J. Thurner, K. L. Turner, and P. K. Hansma, "Design and modeling of a high-speed AFM-scanner," IEEE Trans. Control Syst. Technol. **15**(5), 906–915 (2007).
[27]G. Schitter, W. F. Rijkee, and N. Phan, "Dual actuation for high-bandwidth nanopositioning," in *47th IEEE Conference on Decision and Control, 2008. CDC 2008* (IEEE, 2008), pp. 5176–5181.
[28]S. Wadikhaye, Y. K. Yong, and S. O. R. Moheimani, "A serial-kinematic nanopositioner for high-speed AFM," Rev. Sci. Instrum. **85**(10), 105104 (2014).
[29]B. J. Kenton and K. Leang, "Design, characterization, and control of a monolithic three-axis high-bandwidth nanopositioning stage," in *American Control Conference*, *Baltimore, MD, USA* (IEEE, 2010).
[30]S. Wadikhaye, Y. K. Yong, and S. O. R. Moheimani, "Design of a compact serial-kinematic scanner for high-speed atomic force microscopy: An analytical approach," Micro Nano Lett. **7**(4), 309–313 (2012).
[31]R. J. Roark, W. C. Young, and R. G. Budynas, *Roark's Formulas for Stress and Strain*, 7th ed. (McGraw-Hill, New York, 2002).
[32]G. M. Clayton, C. J. Dudley, and K. K. Leang, "Range-based control of dual-stage nanopositioning systems," Rev. Sci. Instrum. **85**(4), 045003 (2014).
[33]T. Tuma, W. Haeberle, H. Rothuizen, J. Lygeros, A. Pantazi, and A. Sebastian, "Dual-stage nanopositioning for high-speed scanning probe microscopy," IEEE/ASME Trans. Mechatronics **19**(3), 1035–1045 (2014).
[34]A. J. Fleming, "Quantitative scanning probe microscope topographies by charge linearization of the vertical actuator," Rev. Sci. Instrum. **81**(10), 1–5 (2010).

Reuse of AIP Publishing content is subject to the terms at: https://publishing.aip.org/authors/rights-and-permissions. Download to IP: 134.148.193.166 On: Mon, 08 Aug 2016 05:17:24